Title

Dynamic Evolution of Copper Nanowires during CO2 Reduction Probed by Operando Electrochemical 4D-STEM and X–ray Spectroscopy

Journal

Journal of the American Chemical Society, 146(33)

ISSN

0002-7863

Authors

Yang, Yao

Shi, Chuqiao

Feijóo, Julian

et al.

Publication Date

2024-08-21

DOI

10.1021/jacs.4c06480

Peer reviewed

Dynamic Evolution of Copper Nanowires during CO_2 Reduction Probed by *Operando* Electrochemical 4D-STEM and X-ray Spectroscopy

Yao Yang,[1,2,3,4,*,†] Chuqiao Shi,[5,†] Julian Feijóo,[1,4]

Jianbo Jin,[1] Chubai Chen,[1,4] Yimo Han,[5,*] Peidong Yang[1,4,6,7,*]

[1]Department of Chemistry, University of California, Berkeley, CA 94720, USA

[2]Department of Chemistry and Chemical Biology, Cornell University, NY 14850, USA.

[3]Miller Institute for Basic Research in Science, University of California, Berkeley, CA 94720, USA.

[4]Chemical Sciences Division, Lawrence Berkeley National Laboratory, Berkeley, CA 94720, USA.

[5]Department of Materials Science and NanoEngineering, Rice University, Houston, TX 77005, USA.

[6]Department of Materials Science and Engineering, University of California, Berkeley, CA 94720, USA.

[7]Kavli Energy NanoScience Institute, Berkeley, CA 94720, USA.

*Corresponding authors: p_yang@berkeley.edu; yaoyang@cornell.edu; yh76@rice.edu

†Y.Y. and C.S. contributed equally.

Abstract:

Nanowires have emerged as an important family of one-dimensional (1D) nanomaterials owing to their exceptional optical, electrical, and chemical properties. In particular, Cu nanowires (NWs) show promising applications in catalyzing the challenging electrochemical CO_2 reduction reaction (CO_2RR) to valuable chemical fuels. Despite early reports showing morphological changes of Cu NWs after CO_2RR processes, their structural evolution and the resulting exact nature of active Cu sites remain largely elusive, which calls for the development of multimodal *operando* time-resolved nm-scale methods. Here, we report that well-defined 1D copper nanowires, with a diameter of around 30 nm, have a metallic 5-fold twinned Cu core and around 4 nm Cu_2O shell. *Operando* electrochemical liquid-cell scanning transmission electron microscopy (EC-STEM) showed that as-synthesized Cu@Cu_2O NWs experienced electroreduction of surface Cu_2O to disordered (spongy) metallic Cu shell (Cu@Cu^S NWs) under CO_2RR relevant conditions. Cu@Cu^S NWs further underwent a CO-driven Cu migration leading to a complete evolution to polycrystalline metallic Cu nanograins. *Operando* electrochemical four-dimensional (4D) STEM in liquid, assisted by machine learning, interrogates the complex structures of Cu nanograin boundaries. Correlative *operando* synchrotron-based high-energy-resolution X-ray absorption spectroscopy unambiguously probes the electroreduction of Cu@Cu_2O to fully metallic Cu nanograins followed by partial reoxidation of surface Cu during post-electrolysis air exposure. This study shows that Cu nanowires evolve into completely different metallic Cu nanograin structures supporting the *operando* (operating) active sites for the CO_2RR.

Introduction:

Nanowires are one-dimensional (1D) nanostructures with a diameter of 1-100 nm and a large aspect ratio. Over the past three decades, nanowires have emerged as one of three major families of nanomaterials: 0D nanocrystals (e.g. quantum dots, C_{60}), 1D nanowires and carbon nanotubes, and 2D materials (e.g. graphene).[1-3] Nanowires, with their unique size- and dimensionality-dependent physical and chemical properties, have demonstrated a wide range of promising applications in nanolasers,[4] photonics,[5] electronics,[6] energy storage (batteries)[7] and (photo)electrochemical catalysis.[8,9] Elucidating the reaction mechanisms and structures of electrocatalysts is crucial for advancing renewable energy technologies, in particular the electrochemical CO_2 reduction reaction (CO_2RR), which offers a direct route to reducing greenhouse gases to valuable chemical fuels.[10,11] The primary challenge facing the CO_2RR is to develop low-overpotential and high-selectivity electrocatalysts.[12] Cu nanocatalysts are among the few catalyst candidates that can produce multicarbon products at appreciable rates.[13] Early studies on Cu nanowires with diameters from hundreds of nanometers to micrometers explored their applications in the CO_2RR to CO or hydrocarbon products.[14-17] In 2017, our group reported the first example of Cu nanowires (diameter < 100 nm) for the CO_2RR.[18] Pristine ultrathin Cu nanowires with a diameter of ~20 nm and well-defined twin grain boundary, showed a mild structural fracturing while Cu nanowires, wrapped with a graphene oxide protection layer, showed no morphological change after long-term CO_2RR electrolysis. Recent studies on Cu nanowires have shown structural evolution after the electrochemical activation process.[19] Although those *ex situ* studies indicate some levels of structural changes of Cu nanowires after the CO_2RR, the dynamic evolution from pristine Cu nanowires to active Cu sites warrants an *operando* study of electrocatalysts under the reaction conditions.[20,21] *Operando* electrochemical liquid-cell scanning transmission electron microscopy (EC-STEM) enables quantitative electrochemistry and quantitative STEM-based imaging, spectroscopy, and diffraction analysis.[22,23] *Operando* electrochemical 4D-STEM in liquid shows the potential to resolve complex structures of dynamic catalysts under reaction conditions.[24] Correlative synchrotron-based X-ray methods can track dynamic changes in valence state during the electroreduction-reoxidation cycle of electrocatalysts.[25,26] Here, we apply multimodal *operando* methods to investigate the structural evolution and active structure of Cu NWs.

Results & Discussion:

Fig. 1a schematically summarizes the key findings in stepwise evolution pathways of Cu NWs under CO_2RR-relevant conditions. As-prepared Cu NWs, when exposed to air, have a Cu_2O shell (labeled as Cu@Cu_2O NWs), which undergo electroreduction to disordered (spongy) metallic Cu shell (Cu@Cu^S) (Stages 1-2). Cu migrates from surface Cu shell to nucleate and grow into seeds of Cu nanograins (Stages 3-4) followed by continuous growth with Cu atoms from the metallic Cu NW core materials (Stage 5). Overall, pristine Cu@Cu_2O NWs experience complete structural evolution to polycrystalline metallic Cu nanograins under CO_2RR-relevant conditions.

Copper nanowires (NWs) were prepared by colloidal synthesis as a model system to investigate the dynamic evolution of 1D nanocatalysts under electrochemical conditions. High-angle annular dark-field STEM (HAADF-STEM) images of as-synthesized copper NWs show a diameter of 30 ± 10 nm and a length over 3 μm with an aspect ratio of over 100 (Figs. 1b, S1). Atomic-scale HAADF-STEM images exhibit a metallic Cu core with d-spacings of Cu{200} (1.8 Å) surrounded by polycrystalline Cu_2O shell with d-spacings of Cu_2O{111} (2.5 Å) (Figs. 1c, S1-S2). Enlarged atomic-scale STEM images of the Cu core demonstrate the hexagonal symmetry of the face-centered cubic (fcc) Cu near the $[1\bar{1}0]$ zone axis (Figs. 1d, S2). The corresponding Fourier transform shows typical d-spacings of metallic {111} (2.1 Å) and Cu{002} (1.8 Å) (Fig. 1e). Those atomic-scale STEM images of the metallic Cu NW core match well the typical 5-fold twinned structure of Cu NWs with {100} side facets along the <110> axial growth direction (Fig. 1f). STEM based electron energy loss spectroscopy (EELS) was performed to measure the thickness and electronic structure of surface oxide shell (Figs. 1g-l). STEM-EELS elemental maps show a uniform oxide shell in green around the metallic Cu core in yellow. The corresponding EELS line profile, extracted from the dashed white box in Fig. 1g, measures an oxide shell of around 4 nm, i.e. Cu@Cu_2O NWs have the Cu core with an average diameter of around 22 nm surrounded by around 4 nm oxide shell (Figs. 1g, S3-S5). EELS spectra analyze the electronic structure and unambiguously show that the Cu core is metallic with a lower L_3 edge and a delayed L_2 edge due to the fully occupied d orbitals[27] while the shell is Cu_2O with a pronounced L_2 edge at ~960 eV (labeled with asterisk, Figs. 1h, S6). Both EELS and synchrotron X-ray spectroscopy in later discussions rule out the presence of CuO in pristine copper NWs (Figs. S6, S23). Those atomic-scale STEM images and EELS analysis of as-synthesized copper NWs show a Cu@Cu_2O core-shell structure with an average diameter of 30 nm and about 4 nm Cu_2O shell.

The CO_2RR performance of Cu@Cu_2O NWs exhibits an activation period with the Faradaic efficiency (FE) of C_2H_4 reaching a steady state after 1 h CO_2RR electrolysis in an H-cell (Fig. S7a). The CO_2RR product distribution and potential-dependent FE were summarized in Figs. S7b-c. *Ex situ* SEM images showed that Cu@Cu_2O NWs experienced a complete evolution to Cu nanograins at adjacent locations after CO_2RR electrolysis in an H-cell for 1 h (Fig. S8). Those *ex-situ* measurements of copper NWs before and after CO_2RR electrolysis provide a baseline understanding for in-depth *operando* studies of the dynamic evolution of Cu NWs under reaction conditions. *Operando* EC-STEM imaging was performed to investigate dynamic morphological changes of Cu@Cu_2O NWs under electrochemical conditions. A cyclic voltammetric (CV) profile of Cu@Cu_2O NWs shows a well-defined redox couple of Cu/Cu_2O in the EC-STEM setup (Fig. S9) and matches well with the results of Cu nanocatalysts in a standard H-cell.[12] A linear sweep voltammetry (LSV) from 0.4 to around 0 V vs. RHE was performed to trigger the formation of H_2 bubbles (a natural side product during the CO_2RR, Fig. S7b). The electrogenerated H_2 bubbles enable a thin-liquid configuration (~100 nm), which significantly improves spatial resolution while allowing electrolytes to remain electrochemically accessible for subsequent *operando* EC-STEM studies under CO_2RR-relevant conditions.[28] Control experiments showed that Cu@Cu_2O NWs, located on the carbon WE, experienced electroreduction of the surface Cu_2O to

disordered/amorphous (spongy) Cu shell (labeled as $Cu@Cu^S$, Fig. S10). In comparison, $Cu@Cu_2O$, located off the carbon WE, remained largely unchanged, suggesting that the evolution from $Cu@Cu_2O$ to $Cu@Cu^S$ was driven by electrochemical potentials rather than beam-induced damage. Correlative *operando* X-ray absorption spectroscopy of $Cu@Cu_2O$ NWs provides compelling evidence that surface Cu_2O of NWs was reduced to metallic Cu at 0 V (Fig. S11), which indicates the spongy Cu shell observed in EC-STEM achieved a fully metallic state at 0 V and remained metallic through the course of CO_2RR.

Operando EC-STEM movies were acquired to track the dynamic evolution of $Cu@Cu^S$ under electrochemical conditions. Given the rapid morphological evolution of Cu NWs, *operando* EC-STEM was performed at a mild chronoamperometric (CA) experiment under a constant potential of 0 V to capture structural changes in detail (Fig. 2). A beam-dose control experiment was routinely performed to acquire EC-STEM movies without applying electrochemical potentials, corresponding to the "counting-down" time of -40 to 0 s in Movie S1. A reducing potential was applied at 0 s to initiate the dynamic evolution of $Cu@Cu^S$ NWs (Fig. 2a). During the first 4 s, Cu nanograins started nucleating at adjacent locations as shown in two Cu nanograin seeds in the dashed circle and hexagon with $Cu@Cu^S$ showing little morphological changes (Fig. 2b). From 4 to 20 s, $Cu@Cu^S$ showed a progressive and mild fragmentation with nearby Cu nanograins continuing to grow in both sizes and numbers (Figs. 2b-f). From 20 to 40 s, $Cu@Cu^S$ experienced a significant fragmentation of the spongy Cu shell and the Cu NW core with Cu migration to adjacent newly formed as well as existing Cu nanograins (Figs. 2f-k). From 40 to 120 s, $Cu@Cu^S$ achieved a complete evolution to metallic Cu nanograins with no significant further change; This steady-state structure is shown in the false-color comparison of initial $Cu@Cu^S$ NWs in red and Cu nanograins in green (Fig. 2l). *Operando* EC-STEM images were acquired in another region before and after the CA experiment without acquiring continuous EC-STEM movies thus minimizing beam exposure to two imaging frames, which also showed a complete evolution from $Cu@Cu^S$ NWs to polycrystalline Cu nanograins (Fig. S12). Additional *operando* EC-STEM images acquired at -1 V showed that Cu nanograins achieved a steady-state polycrystalline structure with a size of around 50 nm (Figs. S13). A close examination of Cu nanograins formed at -1 V in *operando* EC-STEM shows a high degree of similarity to Cu nanograins observed in *ex situ* STEM and SEM images of NW-derived Cu nanograins after the CO_2RR electrolysis in H-cell (Figs. S14, S8). It indicates that the dynamic evolution of Cu NWs in *operando* EC-STEM can faithfully represent the overall structural changes of Cu NWs in a realistic CO_2RR electrolysis device. It should be noted that *operando* EC-STEM experiments occurred on a significantly shorter timescale (around 1 min) in Fig. 2, when compared to hour-long operation required for $Cu@Cu_2O$ NWs to achieve a steady-state performance in a standard H-cell (Fig. S7), which is likely due to a much stronger electrical field in the confined environment of the EC-STEM.[29,30]

The complex polycrystalline structures of NW-derived Cu nanograins require an in-depth structural analysis in liquid under reaction conditions since Cu nanograins will not maintain the same metallic phase under post-electrolysis air exposure. Four-dimensional (4D) STEM, enabled

by a new-generation electron microscope pixel array detector (EMPAD),[31,32] records a 2D reciprocal-space electron diffraction pattern rapidly at each pixel of the 2D real-space image with a single-electron sensitivity and high dynamic range (Movie S2). *Operando* electrochemical 4D-STEM can reliably retrieve structural information of those NW-derived Cu nanograins at a low beam dose of ~20 e/Å^2 in liquid under reaction conditions.[24] Large 4D-STEM datasets were segmented as different clusters through an unsupervised machine learning method, a K-means based hierarchical clustering method,[33,34] which shed light into the extremely complex structures of nanograin boundaries. Although HAADF-STEM image of the Cu@Cu^S NWs shows a similar image contrast between the Cu core and surface spongy Cu shell (Fig. 3a), the false-color 4D-STEM clustering map of the Cu@Cu^S NWs reveals a clear heterogeneous distribution of Cu nanograins along the Cu@Cu^S wires (Fig. 3b). The colors of black and grey with numbers of 0 and 1, respectively, represent the SiN_x/liquid background and amorphous region on the samples, respectively (Fig. 3c). Other colors from purple to yellow with numbers from 2 to 9 represent crystalline Cu nanograins with different crystal orientations. A region enlarged from the white box (Fig. 3b, inset) highlights an example of one nanograin boundary between two grains with different crystal orientations, grain 1 (G1) in red and grain 2 (G2) in blue, which are surrounded by disordered and spongy Cu shell (Cu@Cu^S). A detailed analysis of nanograin boundaries and corresponding electron diffraction patterns of grain boundaries at each pixel were included in Figs. S15-S16. 4D-STEM clustering map in another region shows various nanograin boundaries surrounded by a thicker disordered and spongy Cu shell (Fig. S17). Although Cu nanograins in colors of 2 to 9 are crystalline, relative to those disordered nanograins in grey with a number of 1, the number of 9 does not necessarily represent a higher order of crystallinity than that of 2. To quantify the relative degree of crystallinity, the fluctuation electron microscopy (FEM) analysis was performed by measuring the medium-range ordering (MRO) and calculating the level of fluctuations (standard deviation) of the diffraction intensity.[35] The FEM map of Cu@Cu^S clearly shows a more crystalline Cu NW core surrounded by a disordered and spongy Cu shell (Figs. S17-18).

Operando electrochemical 4D-STEM was further performed on NW-derived Cu nanograins after achieving a steady-state structure under electrochemical conditions (Figs. 3d-g, S19). Three Cu nanograins were selected to highlight the heterogeneous grain distributions among the complex structures of polycrystalline Cu nanograins. Three regions of the Cu nanograin in Fig. 3e were labeled with red, green, and orange boxes. In particular, the four individual Cu sub-domains at each pixel within the red box in Fig. 3e show distinctly different crystal orientations. The FEM analysis of the same Cu nanograin (e) suggests that Cu domains in colors from purple to orange (numbers from 2 to 6) show a higher degree of crystallinity (Fig. S20). A similar 4D-STEM clustering and FEM analysis were performed on Cu nanograins (f) and (g) (Figs. 3f-g, S21-22). In summary, *operando* EC-STEM and machine-learning-driven 4D-STEM clustering analysis offer a reliable structural analysis of individual Cu nanograins under CO_2RR-relevant conditions. Cu@Cu^S NWs have crystalline NW core surrounded by disordered and spongy shells and the

steady-state NW-derived Cu nanograins are polycrystalline metallic active sites with various nanograin boundaries.

This study further advances our understanding of the dynamic evolution of Cu nanowires by performing *operando* synchrotron-based X-ray spectroscopy (XAS) studies of a large ensemble of Cu@Cu_2O NWs (Fig. 4). High-energy-resolution fluorescence-detected (HERFD) XAS is capable of resolving the pre-edge regions of X-ray absorption near-edge structure (XANES) with a significantly higher energy resolution (around 0.5 eV) of first-row transition metals, when compared to around 1.5 eV energy resolution of conventional XAS in transmission or fluorescence mode (Fig. S23).[23] HERFD XANES of pristine Cu@Cu_2O NWs suggest a mixed phase of Cu and Cu_2O without the presence of CuO (Fig. S23). The quantitative linear combination fitting (LCF) analysis of pristine Cu@Cu_2O NWs calculates a relative fraction of 68% Cu and 32% Cu_2O with a fitting error of 3% (Fig. S24a). To validate the XAS quantification of the oxide fraction, a simplified calculation based on the core-shell geometry of NWs predicts an oxide shell of around 3 nm, which is consistent with the experimental STEM-EELS mapping of around 4 nm Cu_2O shell (Fig. S24b). *Operando* HERFD XANES of Cu@Cu_2O NWs under CO_2RR at -1 V shows the electroreduction of surface Cu_2O to metallic Cu based on a negative shift of the pre-edge energy at around 8980 eV (dashed black box) as well as an increase of the post-edge feature at around 9024 eV (Figs. 4a, S25a). *Ex situ* HERFD XANES spectra of NW-derived Cu nanograins show the progressive reoxidation of surface metallic Cu to Cu_2O under post-electrolysis air exposure (Fig. 4b, S25b). HERFD XANES spectra of the dynamic electroreduction-reoxidation cycle of Cu@Cu_2O NWs are summarized together with bulk Cu and Cu_2O reference spectra in Figs. 4c. The corresponding quantification of the relative fraction of metallic Cu suggests that Cu@Cu_2O NWs achieves fully metallic Cu nanograins with a metallic Cu fraction of 100 ± 1% under CO_2RR at -1 V after 30 min (Fig. 4d), which is consistent with the 1 h timescale of achieving a steady-state CO_2RR performance (Fig. S7). Quantification of post-electrolysis HERFD XANES suggests a decrease in the relative fraction metallic Cu to 79 ± 2% after 40 min air exposure. A relative fraction of 21% Cu_2O of NW-derived Cu nanograins after air exposure is lower than 32% Cu_2O of pristine Cu@Cu_2O NWs, which is consistent with a relatively smaller contribution of surface oxide of a larger size of NW-derived Cu nanograins (~50 nm) when compared to the diameter of pristine NWs (~30 nm). *Operando* extended X-ray absorption fine structure (EXAFS) provides additional information on the coordination environment of Cu as a response to the electroreduction-reoxidation cycle (Fig. S26). To resolve the fast dynamic electroreduction of Cu@Cu_2O NWs,[36] X-ray photon energy was fixed at 8979.5 eV where the change of XANES pre-edge intensity achieved a maximum value and was recorded at a temporal resolution of one second per X-ray acquisition event (Fig. S27). The majority of the 4 nm Cu_2O shell of 1D Cu NWs with a diameter of 30 nm was reduced to metallic Cu after 260 s. In comparison, 0D Cu nanocrystals, with a comparable size of around 30 nm but a thinner Cu_2O shell of around 2 nm require significantly less time of 90 s to reduce the majority of oxide shell (Figs. S27-S28). This comparison indicates that the relative thickness of the Cu_2O shell determines its electroreduction kinetics. In summary, as illustrated in the schematic in Fig. 4d, Cu@Cu_2O NWs experienced a

complete electroreduction of surface Cu_2O to $Cu@Cu^S$ NWs followed by a significant reconstruction to form metallic Cu nanograins under the CO_2RR followed by a partial reoxidation of surface Cu during post-electrolysis air exposure.

In conclusion, this work employed a suite of *operando* methods to elucidate that pristine $Cu@Cu_2O$ NWs experienced the electroreduction of surface Cu_2O shell to a disordered and spongy shell ($Cu@Cu^S$ NWs) followed by a complete evolution to polycrystalline metallic Cu nanograins. As this study reveals how 1D Cu NWs evolve into active Cu nanograins during the CO_2RR, one fundamental challenge facing the development of Cu nanocatalysts is to resolve the molecular picture regarding why Cu atoms migrate during the CO_2RR. We hypothesize that key reaction intermediates, such as adsorbed CO, can trigger CO-driven formation and migration of Cu atoms,[37] leading to a significant structural evolution to polycrystalline Cu nanograins. In this work, *operando* EC-STEM is emerging as a powerful analytical method to enable reliable electrochemistry and simultaneously STEM based imaging and diffraction techniques. *Operando* electrochemical 4D-STEM in liquid, coupled with a machine learning based automated data process, provides valuable insights into the structural analysis of Cu nanograin boundaries. Correlative synchrotron-based X-ray methods provide complementary information on large ensembles of nanocatalysts. We acknowledge that the 4D-STEM clustering is still performed at nanometer-scale in this work to faithfully rule out any undesirable beam damage that may occur at a higher beam dose required for a higher spatial resolution. *Operando* 4D-STEM at/near-atomic scale will provide further information on quantitative analysis of nanograin boundaries and grain size distributions. We anticipate that multimodal *operando* methods can serve as a powerful toolbox to probe complex structures of dynamic catalysts under electrochemical conditions.

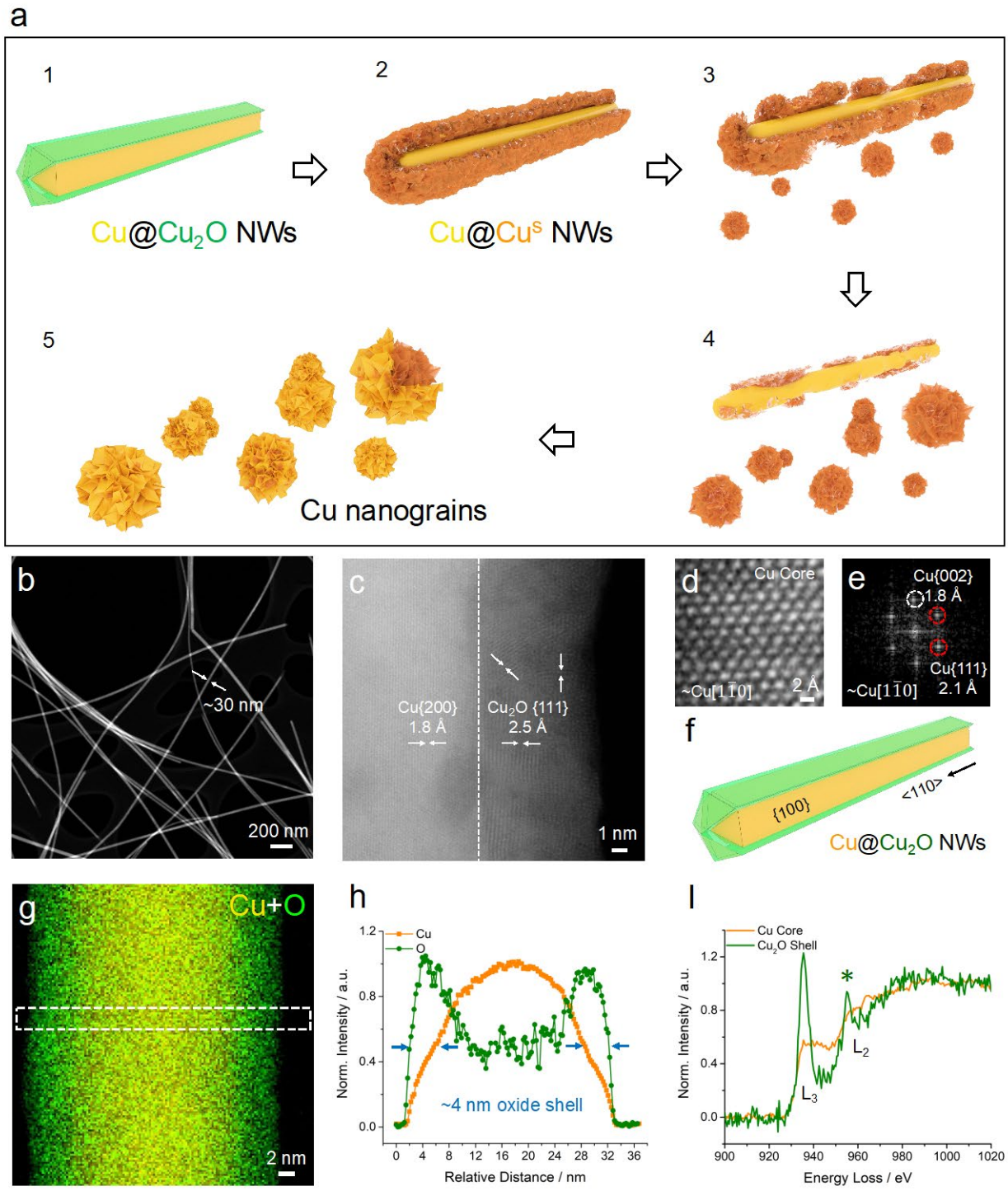

Figure 1. **Schematic of structural evolution and atomic-scale STEM-EELS characterizations of Cu@Cu2O NWs**. (a) Schematic of dynamic evolution of Cu NWs under CO_2RR relevant conditions. (b) HAADF-STEM image of Cu NWs with a diameter of around 30 nm and a length over 3 μm (aspect ratio > 100). (c) Atomic-scale STEM image of metallic Cu core with {200} d-spacings (1.8 Å) surrounded by polycrystalline Cu_2O shell with {111} d-spacings (2.5 Å). (d-e)

Selected atomic-scale STEM image and corresponding Fourier transform (FT) of metallic Cu core with near the [$1\bar{1}0$] zone axis. (f) Schematic showing the typical fivefold twinned structures with {100} side facets. (g-h) STEM-EELS composite mapping and corresponding EELS line profile of Cu@Cu_2O NWs showing around 4 nm oxide shell. (l) EELS spectra of Cu $L_{3,2}$ edges showing the signatures of metallic Cu core in yellow and Cu_2O shell in green.

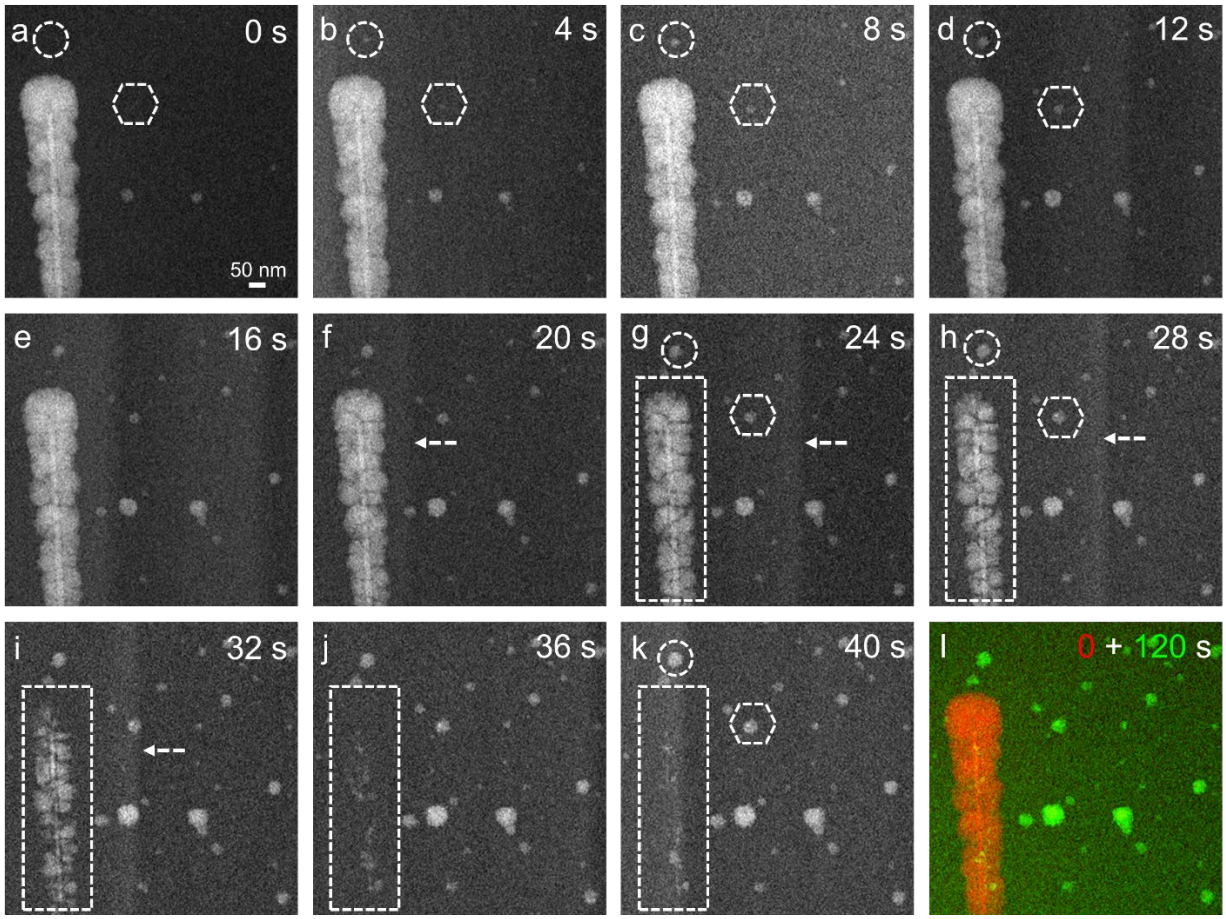

Figure 2. ***Operando*** **EC-STEM images of dynamic evolution of Cu NWs**. (a-f) Nucleation of initial growth of Cu nanograins from metallic Cu NW core surrounded by the spongy Cu shell (Cu@Cu^S) from 0 to 20 s with two Cu nanograin seeds in dashed boxes. (g-k) Significant Cu migration from Cu NWs to form Cu nanograins at adjacent locations from 24 to 40 s. (I) False-color overlay of STEM images acquired at 0 s (red) and after reaching steady-state structures at 120 s (green). The dashed arrows in Figs. f-i mark the non-uniform contrast caused by liquid flow.

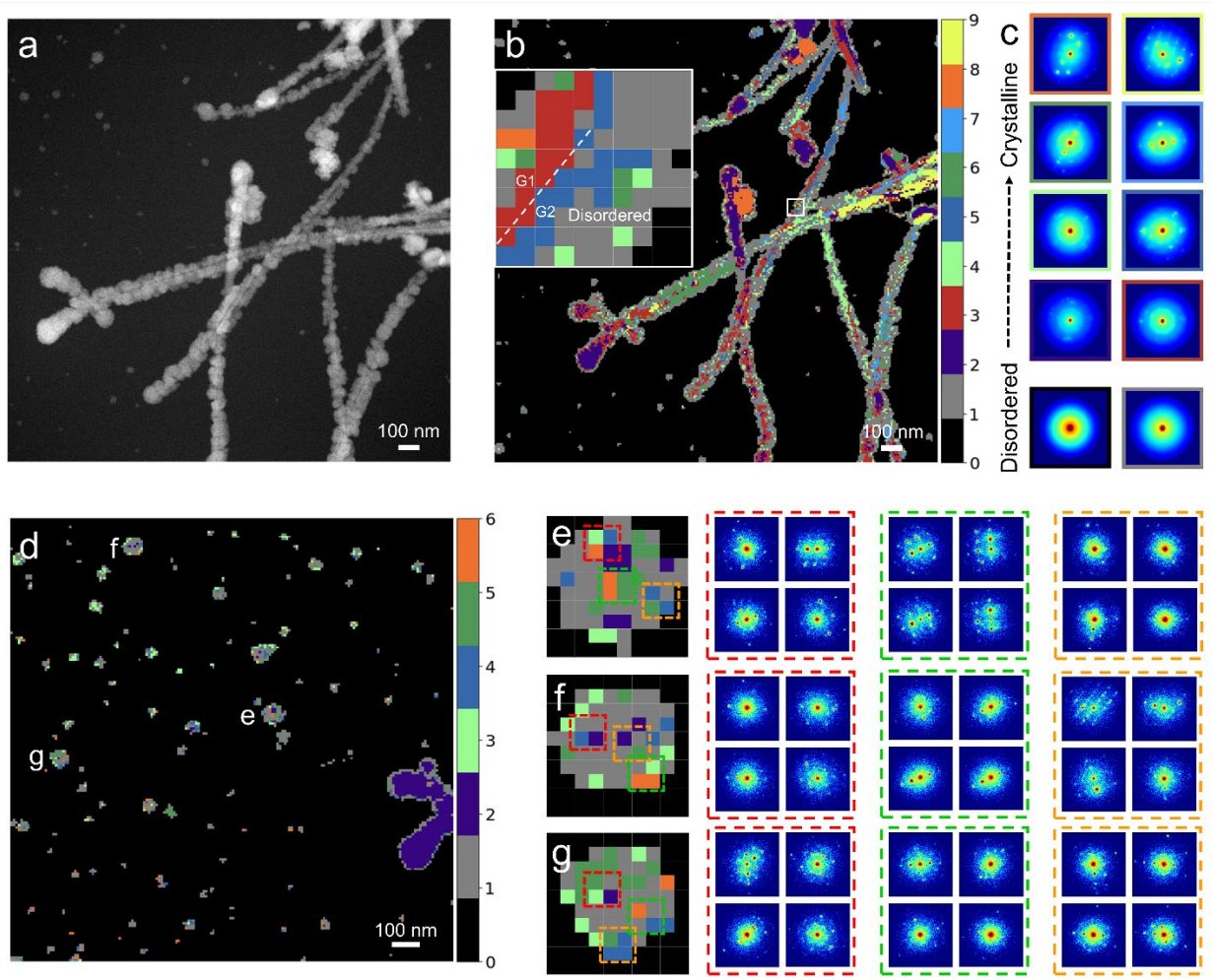

Figure 3. ***Operando*** **electrochemical 4D-STEM in liquid with machine-learning assisted clustering analysis of Cu NWs derived nanograins**. (a-b) *Operando* HAADF-STEM image and the corresponding 4D-STEM clustering map of complex structures of Cu NWs. The false-color 4D-STEM map show of Cu@Cu^S that the crystalline Cu NW core are surrounded by spongy (disordered) Cu shell. (d) *Operando* 4D-STEM clustering map of Cu NWs derived polycrystalline metallic Cu nanograins with selected three Cu nanograins (e-g) for analysis of nanograin boundaries. (e-g) Cu nanograins and corresponding electron diffraction patterns in red, blue and orange regions showing different crystal orientations across grain boundaries.

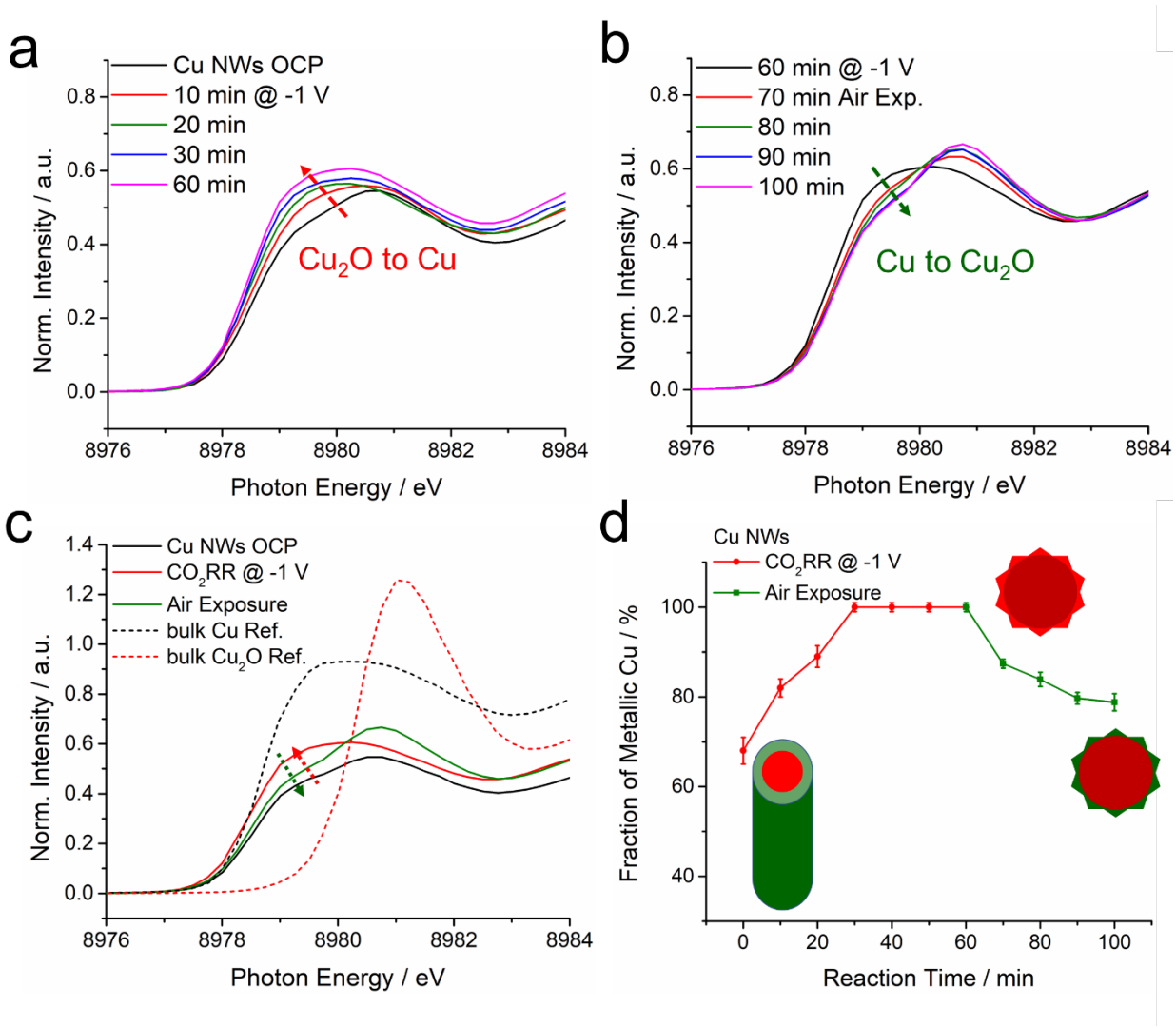

Figure 4. ***Operando*** **high-energy-resolution X-ray absorption spectroscopy studies of dynamic evolution of Cu NWs**. (a) *Operando* HERFD XANES pre-edge spectra of Cu@Cu_2O NWs at the OCP and under steady-state CO_2RR at -1.0 V vs. RHE. Dashed red arrows suggest the progressive increase in pre-edge intensity and negative shift in edge energy values, corresponding to the electroreduction of Cu@Cu_2O NWs to metallic Cu nanograins. (b) *Ex situ* HERFD XANES pre-edge spectra show the partial surface reoxidation of Cu nanograins under post-electrolysis air exposure. (c) Selected XANES spectra of Cu@Cu_2O NWs at the OCP, under the CO_2RR and upon air exposure when compared to bulk Cu and Cu_2O references. (d) Quantitative analysis of the relative fraction of metallic Cu and simplified schematic showing the electroreduction from Cu@Cu_2O NWs, respectively, to fully metallic Cu nanograins followed by subsequent partial oxidation of surface Cu.

Author Information
Corresponding Authors
Peidong Yang; orcid.org/0000-0003-4799-1684
Email: p_yang@berkeley.edu

Yao Yang; orcid.org/0000-0003-0321-3792
Email: yaoyang@cornell.edu

Yimo Han; orcid.org/0000-0003-0563-4611
Email: yh76@rice.edu

Notes
The authors declare no competing financial interests.

Supplementary Information:
Experimental section (synthesis, CO_2RR performance test, *operando* EC-STEM, *operando* HERFD XAS, 4D-STEM clustering and FEM analysis); Figures S1-S22 (*operando* EC- and 4D-STEM, *ex situ* S/TEM analysis and CO_2RR performance); Figure S23-S28 (*operando* HERFD XAS).

Acknowledgement:
This work was supported by the Director, Office of Science, Office of Basic Energy Sciences, Chemical Sciences, Geosciences, & Biosciences Division, of the US Department of Energy under Contract DE-AC02-05CH11231, FWP CH030201 (Catalysis Research Program). *Operando* EC-STEM work was partially supported by the Center for Alkaline-Based Energy Solutions (CABES), an Energy Frontier Research Center (EFRC) program supported by the U.S. Department of Energy, under grant DE-SC0019445. This work used TEM facilities at the Molecular Foundry was supported by the Office of Science, Office of Basic Energy Sciences, of the U.S. Department of Energy under Contract No. DE-AC02-05CH11231. This work made use of TEM facilities at the CCMR which are supported through the National Science Foundation Materials Research Science and Engineering Center (NSF MRSEC) program (DMR-1719875). This work is based on research conducted at the Center for High-Energy X-ray Sciences (CHEXS), which is supported by the National Science Foundation (BIO, ENG and MPS Directorates) under award DMR-1829070. Y.H. and C.S. are supported by NSF CAREER (CMMI–2239545) and Welch Foundation (C-2065). We thank H. Celik and UC Berkeley's NMR facility at the College of Chemistry (CoC-NMR), which is supported in part by NIH S10OD024998. C.C. and J.J. gratefully acknowledge support from Suzhou Industrial Park Scholarships. Y.Y. acknowledges the generous support from the Miller Research Fellowship. We acknowledge the support from Dr. Christopher J. Pollock at Cornell High Energy Synchrotron Source (CHESS).

Reference:

1. Yang, P. 30 Years of Semiconductor Nanowire Research: A Personal Journey. *Isr. J. Chem.* **2023**, e202300127.
2. Yang, P.; Lieber, C. M. Nanorod-Superconductor Composites: A Pathway to Materials with High Critical Current Densities. *Science* **1996**, *273*, 1836-1840.
3. Wu, Y.; Yang, P. Direct Observation of Vapor-Liquid-Solid Nanowire Growth. *J. Am. Chem. Soc.* **2001**, *123*, 3165-3166.
4. Huang, M.; Mao, S.; Feick, H.; Yan, H.; Wu, Y.; Kind, H.; Weber, E.; Russo, R.; Yang, P. Room-Temperature Ultraviolet Nanowire Nanolasers. *Science* **2001**, *292*, 18977-1899.
5. Yan, R.; Gargas, D.; Yang, P. Nanowires Photonics. *Nat. Photonics* **2009**, *3*, 569-576.
6. Jia, C.; Lin, Z.; Huang, Y.; Duan, X. Nanowire Electronics: From Nanoscale to Macroscale. *Chem. Rev.* **2019**, *119*, 9074-9135.
7. Chan, C.; Peng, H.; Liu, G.; Mcilwrath, K.; Zhang, X.; Huggins, R.; Cui, Y. High-Performance Lithium Battery Anodes Using Silicon Nanowires. *Nature Nano.* **2008**, *3*, 31-35.
8. Liu, C.; Tang, J.; Chen, H.; Liu, B.; Yang, P. A Fully Integrated Nanosystem of Semiconductor Nanowires for Direct Solar Water Splitting. *Nano Lett*. **2013**, *13*, 2989-2992.
9. Cestellos-Blanco, S.; Zhang, H.; Kim, J.; Shen, Y.; Yang, P. Photosynthetic Semiconductor Biohybrids for Solar-Driven Biocatalysis. *Nat. Catal*. **2020**, *3*, 245-255.
10. Ross, M. B.; Luna, P. D.; Li, Y.; Dinh, C.-T.; Kim, D.; Yang, P.; Sargent, E. H. Designing materials for electrochemical carbon dioxide recycling. *Nat. Catal*. **2019**, *2*, 648-658.
11. Birdja, Y. Y.; Pérez-Gallent, E.; Figueiredo, M. C.; Göttle, A. J.; Calle-Vallejo, F.; Koper, M. T. M. Advances and challenges in understanding the electrocatalytic conversion of carbon dioxide to fuels. *Nat. Energy* **2017**, *4*, 732-745.
12. Li, Y.; Kim, D.; Louisia, S.; Xie, C.; Kong, Q.; Yu, S.; Lin, T.; Aloni, S.; Fakra, S. C.; Yang, P. Electrochemically Scrambled Nanocrystals Are Catalytically Active for CO_2 -to-Multicarbons. *Proc Natl Acad Sci USA* **2020**, *117*, 9194–9201..
13. Yang, Y.; Louisia, S.; Yu, S.; Jin, J.; Roh, I.; Chen, C.; Fonseca Guzman, M. V.; Feijóo, J.; Chen, P.-C.; Wang, H.; Pollock, C. J.; Huang, X.; Shao, Y.-T.; Wang, C.; Muller, D. A.; Abruña, H. D.; Yang, P. Operando Studies Reveal Active Cu Nanograins for CO2 Electroreduction. *Nature* **2023**, *614*, 262–269
14. Ma, M.; Djanashvili, K.; Smith, W. A. Controllable Hydrocarbon Formation from the Electrochemical Reduction of CO_2 over Cu Nanowire Arrays. *Angew. Chem. Int. Ed*. **2016**, 55, 6680−6684.
15. Xie, M. S.; Xia, B. Y.; Li, Y.; Yan, Y.; Yang, Y.; Sun, Q.; Chan, S. H.; Fisher, A.; Wang, X. Amino acid modified copper electrodes for the enhanced selective electroreduction of carbon dioxide towards hydrocarbons. *Energy Environ. Sci.* **2016**, 9, 1687−1695.
16. Raciti, D.; Livi, K. J.; Wang, C. Highly Dense Cu Nanowires for Low-Overpotential CO_2 Reduction. *Nano Lett*. **2015**, 15, 6829-6835.
17. Cao, L.; Raciti, D.; Li, C.; Livi, K. T.; Rottmann, P. F.; Hemker, K. J.; Mueller, T.; Wang, C. Mechanistic Insights for Low-Overpotential Electroreduction of CO_2 to CO on Copper Nanowires. *ACS Catal.* **2017**, *7*, 8578–8587.
18. Li, Y.; Cui, F.; Ross, M. B.; Kim, D.; Sun, Y.; Yang, P. Structure-Sensitive CO_2 Electroreduction to Hydrocarbons on Ultrathin 5-fold Twinned Copper Nanowires. *Nano Lett.* **2017**, 17, 1312−1317.
19. Choi, C.; Kwon, S.; Cheng, T.; Xu, M.; Tieu, P.; Lee, C.; Cai, J.; Lee, H. M.; Pan, X.; Duan, X.; Goddard III, W.; Huang, Y. Highly active and stable stepped Cu surface for enhanced electrochemical CO_2 reduction to C_2H_4. *Nat. Catal.* **2020**, *3*, 804-812.
20. Yang, Y..; Xiong, Y.; Zeng, R.; Lu, X.; Krumov, M.; Huang, X.; Xu, W.; Wang, H.; DiSalvo, F. J.; Brock, J. D.; Muller, D. A.; Abruña, H. D. *Operando* Methods in Electrocatalysis. *ACS Catal*. **2021**, *11*, 1136-1178.
21. Zhang, Q.; Song, Z.; Sun, X.; Liu, Y.; Wan, J.; Betzler, S. B.; Zheng, Q.; Shangguan J.; Bustillo, K. C.; Ercius, P.; Narang, P.; Huang, Y.; Zheng, H. Atomic Dynamics of Electrified Solid–Liquid Interfaces in Liquid-Cell TEM. *Nature* 2024, 630, 643-647.

22. Holtz, M. E.; Yu, Y.; Gunceler, D.; Gao, J.; Sundararaman, R.; Schwarz, K. A.; Arias, T. A.; Abruña, H. D.; Muller D. A. Nanoscale Imaging of Lithium Ion Distribution during *In Situ* Operation of Battery Electrode and Electrolyte. *Nano Lett*. **2014**, *14*, 1453-1459.
23. Yang, Y.; Shao, Y.-T.; Lu, X.; Abruña, H. D.; Muller, D. A. Metal Monolayers on Command: Underpotential Deposition at Nanocrystal Surfaces: A Quantitative *Operando* Electrochemical Transmission Electron Microscopy Study. *ACS Energy Lett.* **2022**, *7*, 1292-1297.
24. Yang, Y.; Shao, Y.-T.; Lu, X.; Yang, Y.; Ko, H.-Y.; DiStasio, R. A.; DiSalvo, F. J.; Muller, D. A.; Abruña, H. D. Elucidating Cathodic Corrosion Mechanisms with Operando Electrochemical Transmission Electron Microscopy. *J. Am. Chem. Soc*. **2022**, *144*, 15698-15708.
25. Feijóo, J.; Yang, Y.; Guzman, M. F.; Vargas, A.; Chen, C.; Pollock, C. J.; Yang, P. Operando High-Energy-Resolution X-ray Spectroscopy of Evolving Cu Nanoparticle Electrocatalysts for CO_2 Reduction. *J. Am. Chem. Soc*. **2023**, *145*, 20208-20213.
26. Yang, Y.; Roh, I.; Louisia, S.; Chen, C.; Jin, J.; Yu, S.; Salmeron, M. B.; Wang, C.; Yang, P. *Operando* Resonant Soft X-Ray Scattering Studies of Chemical Environment and Interparticle Dynamics of Cu Nanocatalysts for CO_2 Electroreduction. *J. Am. Chem. Soc.* **2022**, *144*, 8927-8931.
27. Egerton, R. F. Electron Energy-Loss Spectroscopy in the Electron Microscope, Springer, 2011, page 231.
28. Yang, Y.; Shao, Y.-T.; Jin, J.; Feijóo, J.; Roh, I.; Louisia, S.; Yu, S.; Fonseca Guzman, M. V.; Chen, C.; Muller, D. A.; Abruña, H. D.; Yang, P. Operando Electrochemical Liquid-Cell Scanning Transmission Electron Microscopy (EC-STEM) Studies of Evolving Cu Nanocatalysts for CO_2 Electroreduction. *ACS Sustain. Chem. Eng.* **2023**, *11*, 4119-4124.
29. Feng, L.; Medvedeva, X. V.; Medvedev, J. J.; Khairullina, E.; Engelhardt, H.; Chandrasekar, S.; Guo, Y.; Jin, J.; Lee, A.; Therien-Aubin, H.; Ahmed, A.; Pang, Y.; Klinkova, A. Interplay of Electrochemical and Electrical Effects Induces Structural Transformations in Electrocatalysts. *Nat. Catal*. **2021**, *4*, 479-487.
30. Yang, Y.; Feijóo, J.; Briega-Martos, V.; Li, Q.; Krumov, M.; Merkens, S.; De Salvo, G.; Chuvilin, A.; Jin, J.; Huang, H.; Pollock, C. J.; Salmeron, M. B.; Wang, C.; Muller, D. A.; Abruña, H. D.; Yang, P. *Operando* Methods: A New Era of Electrochemistry. *Curr. Opin. in Electrochem*. **2023**, *42*, 101403.
31. Tate, M. W.; Purohit, P.; Chamberlain, D.; Nguyen, K. X.; Hovden, R.; Chang, C. S.; Deb, P.; Turgut, E.; Heron, J. T.; Schlom, D. G.; Ralph, D.; Fuchs, G. D.; Shanks, K. S.; Philipp, H. T.; Muller, D. A.; Gruner, S. M. High Dynamic Range Pixel Array Detector for Scanning Transmission Electron Microscopy. *Microsc. Microanal*. **2016**, *22*, 237-249.pge
32. Chen, Z.; Jiang, Y.; Shao, Y.-T.; Holtz, M. E.; Odstrcil, M.; Guizar-Sicairos, M.; Hanke, I.; Ganschow, S.; Schlom, D. G.; Muller, D. A. Electron Ptychorgraphy Achieves Atomic-Resolution Limits Set by Lattice Vibrations. *Science* **2021**, *372*, 826-831.
33. Shi, C.; Cao, M. C.; Rehn, S. M.; Bae, S. H.; Kim, J.; Jones, M. R.; Muller, D. A.; Han, Y. Uncovering Material Deformations via Machine Learning Combined with Four-Dimensional Scanning Transmission Electron Microscopy. *Npj Comput. Mater*. **2022**, *8*, 114.
34. Hartigan, J. A. & Wong, M. A. A K-means Clustering Algorithm. *J. R. Stat. Soc. Ser. C. Appl Stat.* **1979**, *28*, 100–108.
35. Voyles, P. M.; Muller, D. A. Fluctuation Microscopy in the STEM. *Ultramicroscopy* **2002**, *93*, 147-159.
36. Yang, Y.; Wang, Y.; Xiong, Y.; Huang, X.; Shen, L.; Huang, R.; Wang, H.; Pastore, J. P.; Yu, S.-H.; Xiao, L.; Brock, J. D.; Zhuang, L.; Abruña H. D. In Situ X-ray Absorption Spectroscopy of a Synergistic Co-Mn Oxide Catalyst for the Oxygen Reduction Reaction. *J. Am. Chem. Soc*. **2019**, *141*, 1463-1466.
37. Xu, L.; Papanikolaou, K. G.; Lechner, B. A.; Je, L.; Somorjai, G.; Salmeron, M. B.; Mavrikakis, M. Formation of Active Sites on Transition Metals Through Reaction-Driven Migration of Surface Atoms. *Science* **2023**, *380*, 70–76.

Table of Contents